



Influence of stress triaxiality on hydrogen assisted ductile damage in an X70 pipeline steel

Robin Depraetere ^{a,*}, Wim De Waele ^a, Margo Cauwels ^b, Tom Depover ^b, Kim Verbeken ^b, Matthieu Boone ^c, Stijn Hertelé ^a

^a Ghent University, Department of Electromechanical, Systems and Metal Engineering, Technologiepark-Zwijnaarde 46, Zwijnaarde, 9052, Belgium

^b Ghent University, Department of Materials, Textiles and Chemical Engineering, Technologiepark-Zwijnaarde 46, Zwijnaarde, 9052, Belgium

^c Ghent University, Centre for X-ray Tomography, Proeftuinstraat 86, Ghent, 9000, Belgium

ARTICLE INFO

Dataset link: <https://doi.org/10.17605/OSF.IO/WKHG3>

Keywords:

Hydrogen embrittlement
Micro-CT
Ductile fracture
Void shape
Anisotropy
Pipeline steel
X70

ABSTRACT

The presence of hydrogen in steel components affects their structural integrity through a phenomenon called hydrogen embrittlement. While it is known that hydrogen affects the mechanical damage development upon loading, the specific mechanisms are still unclear. An experimental study is presented that investigates the plastic anisotropy and ductile fracture behavior of API 5L X70 pipeline steel with and without hydrogen charging at multiple scales. Three different tensile test specimen geometries (smooth and notched axisymmetric) are employed to investigate the influence of stress triaxiality thereon. The macromechanical responses during tensile tests are analyzed, along with micromechanical features of the resulting damage obtained using High-Resolution X-ray Computed Tomography. For all stress triaxialities tested, the presence of hydrogen does not affect the macroscopic plastic anisotropy, but accelerates ductile damage development and fracture, which is in agreement with the plasticity dominated hydrogen embrittlement mechanisms HELP and HESIV. Increasing stress triaxiality leads to a larger susceptibility to hydrogen embrittlement. Hydrogen accelerated void nucleation and enhanced lateral void growth are observed and quantified. The presented results can aid the development of numerical models describing hydrogen embrittlement in high-strength low-alloy steel.

1. Introduction

Hydrogen will play a key role in the global energy transition. To accommodate this transition, hydrogen will have to be produced, stored and transported on a massive scale. A fraction of the infrastructure to do so already exists, for example the natural gas pipeline network which is typically constructed out of high-strength low-alloy (HSLA) steels of variable characteristics (strength grade, alloying scheme, purity, rolling process, heat treatment...). Of particular concern is the phenomenon of hydrogen assisted mechanical degradation of metals, also known as hydrogen embrittlement (HE). The presence of hydrogen affects the structural integrity of metal components and structures, by reducing their ductility and fracture toughness [1]. While HE has been known for a long time [2] and its reduction of mechanical properties is indisputable, the phenomenon has not been comprehensively explained due to its complexity, reflected in a multitude of possible underlying mechanisms [3,4].

Several theories describing HE have been set forth. They can be categorized into the brittle, and the plasticity dominated mechanisms [5]. Hydrogen Enhanced DEcohesion (HEDE) is the most commonly

adopted brittle mechanism [6] and advocates that hydrogen weakens the cohesive strength of the steel lattice. The plasticity dominated mechanisms include Hydrogen Enhanced Localized Plasticity (HELP) and Hydrogen Enhanced Strain-Induced Vacancies (HESIV). HELP argues that the dislocation mobility is enhanced by the presence of hydrogen. Following this theory, it is argued that quasi-cleavage features on the fracture surface of hydrogen-embrittled steel can be explained by ductile processes that are enhanced by the presence of hydrogen, rather than by a cleavage mechanism [3,7]. On the other hand, HESIV claims that hydrogen enhances the formation of vacancies upon straining as a result of a reduction in the vacancy-formation energy [6,8]. Recently, it has been hypothesized that multiple HE mechanisms could occur simultaneously in a synergistic manner [4].

Analyzing ductile fracture is key to a number of engineering problems [9]. It consists of various stages, starting with voids nucleating around microscopic stress concentrations such as inclusions, precipitates and vacancy clusters [10]. Upon further deformation, these voids will grow and finally coalesce, resulting in final fracture [11]. The presence of hydrogen in steel influences the microscopic void processes,

* Corresponding author.

E-mail address: robidpra.depraetere@ugent.be (R. Depraetere).

as was demonstrated both experimentally [7,12–15], and numerically [16–20].

Comprehension of the interaction of hydrogen with voids is of crucial relevance. First of all, it is instrumental to the fundamental understanding of HE, since the underlying mechanisms are still under debate. Further, it is key to the development of numerical models predicting hydrogen assisted degradation [18]. Particularly, most HELP-based numerical models examine the effect of hydrogen on ductile damage, either on a single void through unit cell analysis [16,18–20], or implicitly using adapted continuum models such as the Gurson model for void growth [21–23] or the fracture strain model [24]. Asadi-poor et al. [25] employed void observations from experimental studies [26,27] to motivate choices during their numerical calibration procedure for modeling tensile tests on hydrogen charged dual-phase steel. In HESIV-based numerical models, the mechanistic effect of hydrogen is incorporated through an increase of the void nucleation parameter [8].

In particular, two aspects in the hydrogen-void interactions are of interest. First, it is experimentally established that hydrogen accelerates one or more of the aforementioned damage processes of void nucleation, growth and coalescence [7,8,12–15], corresponding to the plasticity dominated HE mechanisms HELP and HESIV. In addition to experimental research, multiple numerical studies implemented the HELP mechanism through a local flow stress reduction and observed accelerated void growth and coalescence [16,18–21,28]. While these studies typically use a linear flow stress reduction with increasing hydrogen concentration as postulated by Sofronis et al. [29], it must be emphasized that this law is of phenomenological nature and experimental evidence is lacking. As such, results obtained using such approach could be debatable [18,20].

A second aspect of the hydrogen-void interactions is the potentially affected void shape. The effect of void shape on ductile fracture without hydrogen is extensively analyzed using numerical void cell models [11,30]. The consensus is that for low stress triaxialities, differences in initial void shape can have a large effect on the overall ductility, while for higher stress triaxialities this effect disappears. Matsuo et al. [15] performed tensile tests on uncharged and hydrogen charged smooth round bar tensile specimens of pipeline steel JIS-SGP. Hydrogen enhanced lateral void growth was observed, resulting in an accelerated coalescence. This observation was qualitative and not quantified. In an attempt to reproduce this effect in numerical simulations, Yu et al. [18] changed the linear softening law into a sigmoidal law, since the former could not capture hydrogen enhanced lateral void growth. The authors reported that their improved type of law is still phenomenological due to the lack of experimental evidence, but is probably closer to reality. To the authors' knowledge, a quantitative analysis of hydrogen enhanced lateral void growth in HSLA steel is not found in literature.

In addition, considering that only smooth round bar tensile specimens were targeted in the study of Matsuo et al. [15], experimental studies investigating the impact of stress triaxiality on the aspects above are lacking as well.

Assessing the evolution of damage is required to understand the ductile fracture process. This is typically done using two-dimensional metallographic sections [14,31,32]. More recently, High-Resolution X-ray Computed Tomography (micro-CT) has been utilized for investigating ductile damage in a quantitative way [33–36]. It has the advantage of providing three-dimensional information in a non-destructive manner. Since the results are quantitative, they can be employed for determining parameters in porosity-based continuum models [34,37,38].

In the context of hydrogen-void interactions, X-ray micro-CT was used by Morrissey et al. [27] to analyze the effect of hydrogen charging in ferritic stainless steel, without any mechanical loading. They observed an increase in initial void volume fraction due to hydrogen charging. Maire et al. [26] investigated hydrogen-void interactions in austenitic stainless steels in terms of void nucleation, growth and void shape using X-ray micro-CT. While the void nucleation and

growth were unaffected by hydrogen charging, it was demonstrated that the shape of nucleated voids was changed from spherical cavities to micro-cracks oriented perpendicular to the loading direction.

To the authors' knowledge, no X-ray micro-CT studies have been performed on hydrogen charged HSLA steel. Furthermore, a quantitative investigation of the fracture mechanisms over various triaxialities in a hydrogen charged steel with banded microstructure is lacking. The goal of the present work is to combine X-ray micro-CT with macroscopic mechanical testing (in absence and presence of hydrogen charging) to assess the effect of hydrogen on the plastic anisotropy and the ductile damage processes: void nucleation, growth and coalescence. For this purpose, tensile tests have been carried out on API 5L X70 [39] pipeline steel with and without hydrogen charging. API 5L X70 falls under the category of HSLA steels, and is a commonly used steel grade within the existing natural gas pipeline grid. The influence of stress triaxiality on the structural behavior is examined by testing different specimen geometries. X-ray micro-CT has been performed on a representative subset of the experiments. The work presents quantitative results where deemed possible, and qualitative results elsewhere.

2. Materials & methods

2.1. Materials

The investigated material is a grade API 5L X70 [39] pipeline steel that had been in service for around 30 years. It was produced by a thermomechanically controlled rolling process (TMCP), resulting in a banded ferrite–pearlite microstructure and a notable degree of plastic anisotropy [40]. The microstructure is shown in Fig. 1 and features MnS inclusions that are elongated in the longitudinal (L) and transverse (T) direction. In the center region, the microstructure is characterized by a pearlite fraction of $13.3 \pm 1.9\%$, and an average grain size of $4.88 \pm 0.82 \mu\text{m}$. The chemical composition, as measured by spark source optical emission spectroscopy (SS-OES) is given in Table 1. The pipe has an outside diameter of 1016 mm and a measured wall thickness of 15.8 mm. A more detailed microstructural characterization of the tested material can be found in Cauwels et al. [41].

Smooth and double-notched axisymmetric tensile specimens were extracted from the pipe, with the loading axis oriented in the longitudinal (L) direction (Fig. 2). The smooth tensile specimen is further denoted as R₀₀, and the double-notched specimens feature notches with a radius of 2 mm or 6 mm, further referred to as R2 and R6 respectively. By employing three different geometries, different levels of positive stress triaxialities are obtained. The initial stress triaxiality at the center can be calculated using Bridgman's formula [42] as 0.89, 0.56 and 0.33 for R2, R6 and R₀₀ respectively. Notably, these triaxiality levels will slightly vary upon the development of plasticity, as discussed in [40]. The use of two notches allows the microscopic assessment of damage at two different deformation states: complete failure and maximum load [43].

2.2. Ex-situ tensile testing after hydrogen charging

The hydrogen charging of tensile specimens was performed using an electrochemical charging method. Prior to the tensile test, the specimens were submerged in an electrolyte ($0.5 \text{ M H}_2\text{SO}_4$ with 1 g/l of thiourea) and a current density of 0.8 mA/cm^2 was applied. Experiments showed that charging with these conditions for six hours resulted in a saturated hydrogen concentration of $0.89 \pm 0.15 \text{ wppm}$ throughout the specimen, measured with hot extraction at 300°C (G8 Galileo) using the thermal conductivity detector (TCD) for hydrogen detection. Importantly, it was also confirmed that these charging conditions do not induce Hydrogen Induced Cracking (HIC) for the investigated material, which would invalidate the mechanical test results [41].

After charging, the specimens were mounted in a servo-hydraulic test rig, and a fixed displacement rate was applied. A strain rate of

Table 1
Average chemical composition of the investigated steel in weight percentage.

Material	Fe	C	Mn	Si	Cr	Ni	Nb	V	Mo	Cu	S	P
API 5L X70	97.534	0.108	1.633	0.426	0.030	0.022	0.054	0.068	0.002	0.018	0.003	0.015

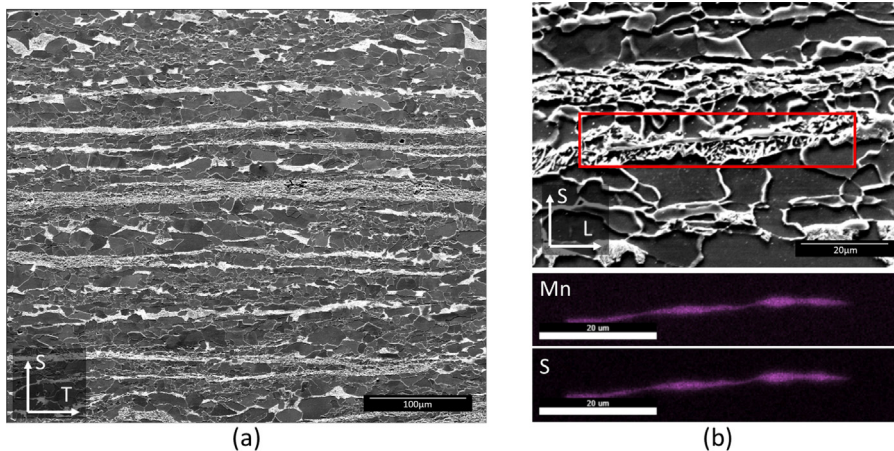


Fig. 1. Scanning electron microscopy images illustrating (a) the banded ferrite–pearlite microstructure, and (b) an elongated MnS inclusion, with energy-dispersive X-ray analysis (EDX) below.

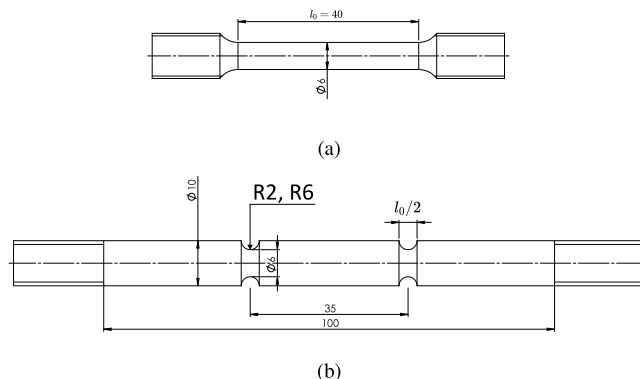


Fig. 2. Specimen geometry of (a) the smooth round bars (R_{∞}) and (b) the double-notched round bars (R_2 and R_6). Dimensions in millimeter.

$2.5 \times 10^{-4} \text{ s}^{-1}$ was adopted, where the gauge length used for calculating the strain rate corresponds to the total length of the reduced section(s) (l_0 in Fig. 2). Note that upon necking of one of the two notches, all deformation will concentrate here, resulting in a local doubling of the strain rate in this notch.

Since hydrogen is continuously effusing out of the specimen, each tensile test was started seven minutes (plus/minus one second) after the charging process was stopped. A prior numerical study using the measured diffusivity coefficient of the material showed that the combination of the sample manipulation time and the test duration does not significantly affect the hydrogen content in the center of the specimen (<5% based on a numerical analysis representative for worst-case conditions), where crack initiation due to ductile damage is expected.

To investigate the evolution of damage at different strain levels, three interrupted tests were performed for each specimen geometry. In addition, two specimens for each geometry were tested until complete fracture. In the interrupted tests, the specimens were unloaded after an intended displacement was obtained. Additionally to these hydrogen charged tests, two tensile tests were performed in air for each notch until complete fracture, serving as a reference. In total, 6 tests were performed in air, and 25 tests were performed after hydrogen charging.

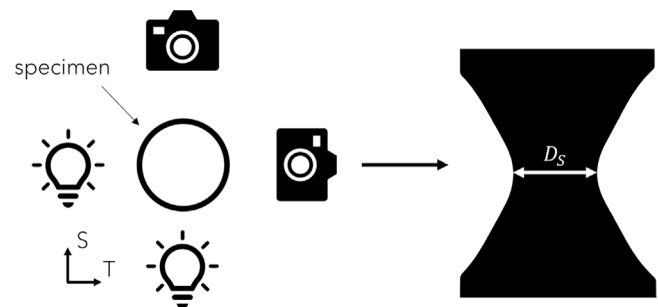


Fig. 3. Top view of setup (left) for monitoring the lateral contractions in the transversal (T) and through-thickness (S) directions [40].

To track the deformation behavior of the specimens during tensile testing, the lateral contraction of the diameter in the transversal (T) and the through-thickness (S) directions was monitored optically using the technique that is schematically shown in Fig. 3 and is described in Depraetere et al. [40]. By using two perpendicularly positioned cameras, both the post-necking behavior as well as the anisotropy of the material can be evaluated during the test [44]. This provides a local measurement of the strain, rather than a non-local measurement of the strain averaged over the gauge length, i.e. when using an extensometer for axial elongation.

The recording of the lateral contractions allows to determine the minimal instantaneous cross-sectional area (in the notch or the necking region of an unnotched specimen) during the tensile test as $A = \pi D_T D_S / 4$. Using the recorded force F , the true stress σ_t and the true strain ϵ_t can be determined:

$$\sigma_t = F / A \quad (1)$$

$$\epsilon_t = \ln(A_0 / A) \quad (2)$$

where A_0 represents the initial minimal cross-sectional area before deformation.

The true strain represents an averaged longitudinal quantity in the minimal section of the notch [11]. The final failure strain is determined as

$$\epsilon_f = \ln(A_0 / A_f) \quad (3)$$

where A_f represents the final area as measured post-mortem on the fracture surface.

The plastic anisotropy is characterized by the Lankford coefficient \mathcal{L} , which is defined as the ratio of the strains perpendicular to the loading direction:

$$\mathcal{L} = \frac{\epsilon_T}{\epsilon_S} = \frac{\ln(D_T/D_0)}{\ln(D_S/D_0)} \quad (4)$$

2.3. High Resolution X-ray Computed Tomography

High Resolution X-ray Computed Tomography (X-ray micro-CT) has been used to quantify damage after deformation. The scans were performed at the high-energy setup HECTOR of the Ghent University Centre for X-ray Tomography [45]. The tube was operated at 200 kV, using a 1 mm Cu filter to reduce beam hardening effects. Depending on the diameter of the region of interest, between 1800 and 2200 projection images were acquired over a full 360° rotation. Tomographic reconstruction was done using the in-house developed software package Octopus Reconstruction. Using geometrical magnification, a reconstructed voxel size of (0.01 mm)³ was achieved. For each notch, one fractured hydrogen charged and one fractured uncharged sample was scanned, together with all samples from the interrupted tests.

Median filtering ($2 \times 2 \times 2$ voxels) and subsequent grayscale thresholding was carried out on the reconstructed grayscale volumes using software 3D slicer (4.11), to separate the voids from the material. By employing the same threshold value, all samples can be compared in a consistent way. Only features that are larger than 5 voxels in volume are considered as voids. The thresholded volumes have been exported to .stl and are available to download [46]. Further analysis with the Python module Trimesh (3.9.7) was performed to characterize each individual void by certain geometrical and spatial quantities.

From the void volume V , the equivalent diameter D_{eq} of a sphere with the same volume is calculated as

$$D_{eq} = \sqrt[3]{\frac{6V}{\pi}} \quad (5)$$

As such, the smallest considered voids have an equivalent diameter of $D_{eq} = 0.021$ mm.

To quantify the void shape, the aspect ratio of each void is determined. Since the material shows a large degree of anisotropy (see further in Section 3), a distinction is made between the longitudinal L , the transversal T and the through-thickness S direction. Aspect ratios dS/dT , dL/dT and dS/dL are calculated, with dL , dS , dT the dimensions of the bounding box of the void along the three respective directions. Keeping in mind that L is the loading direction, these ratios allow to assess whether voids are elongated longitudinally or perpendicularly with respect to the loading direction.

To get an idea of the void development, the local presence of voids can be evaluated against the local strain. Because in porosity-based damage models, the amount of damage at a certain point is solely determined by the plastic strain and the stress triaxiality history, these results can serve as an input for such models [34]. The presence of voids is characterized by the void volume fraction f in each voxel-thick slice perpendicular to the loading direction. It is calculated by dividing the area of the voids by the sum of the void and metal area, similar to Daly et al. [34]. For the smooth round bars ($R\infty$), the local average strain ϵ_{loc} in each slice is calculated using Eq. (2) where A refers to the local area in that cross-sectional slice and is obtained from the processed X-ray volumes. This method is schematically shown in Fig. 4. The data from above and below the minimal cross section is averaged together, and a moving average calculation is applied over 10 slices to get an average view of the void development. It has to be noted that the process of void nucleation occurs at a much smaller scale than the employed resolution. However, the consequences of void nucleation and void growth are visible.

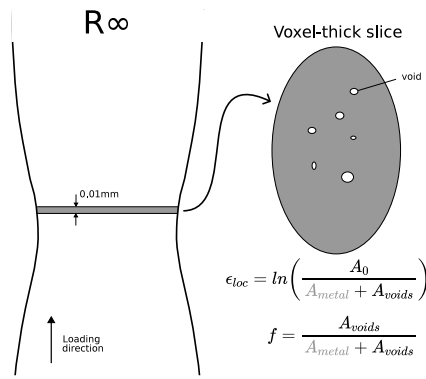


Fig. 4. Schematic of procedure for extracting the local void volume fraction f and the local strain ϵ_{loc} in each slice, for the smooth round bar ($R\infty$).

3. Results

3.1. Macroscopic measurements

The resulting normalized load (Fig. 5(a)) and true stress (Fig. 5(b)) versus true strain curves suggest that the macroscopic specimen strength is insignificantly affected by hydrogen charging for all geometries. In contrast, the loss in ductility is evident. Further, an increase in stress triaxiality causes an increase in maximum normalized load with a reduction in fracture strain, as expected [11]. Both the fully fractured as well as the interrupted specimens are depicted. For the smooth round bars ($R\infty$), there is more variability in the macromechanical curves. This might be attributed to the more stochastic nature of the damage process that exists when there is no predefined failure location, compared to notched round bars where the fracture process is decoupled from plastic instabilities [47].

To quantify the effect of hydrogen on the macroscopic behavior and to relate this to the microscopic fracture processes, the stress versus strain curve (Fig. 5) is typically divided into three stages, with three corresponding deformation states. Refs. [47,48] state that:

1. From the start up to the point of maximum normalized load $(F/A_0)_{max}$ (triangle in Fig. 5(a)), elasticity and plasticity occurs. There is no development of damage yet. While $(F/A_0)_{max}$ is a measure for the strength of the material, the corresponding strain ϵ_t relates to the ductility. The latter is also called ‘uniform elongation’ for smooth round bars, when converted to engineering strain.
2. From the point of maximum normalized load to the point of maximum true stress $\sigma_{t,max}$ (square in Fig. 5), void nucleation starts to occur with subsequent void growth. A few isolated void coalescence events might initiate. The occurrence of $\sigma_{t,max}$ is also exposed by a sudden change in slope of the normalized load versus strain curve (square in Fig. 5(b)) and is associated with the initiation of a macroscopic crack in the center of the specimen [11,47,49]. For this reason, the true strain ϵ_t at $\sigma_{t,max}$ is further referred to as the critical strain ϵ_c .
3. From the critical strain ϵ_c up to the fracture strain ϵ_f , the macroscopic crack propagates until complete fracture.

Table 2 summarizes these characteristic deformation states for each notch configuration and each test condition (charged versus uncharged). It has to be noted that the interrupted tests evidently do not have a final fracture strain, and that some interrupted tests did not even reach $\sigma_{t,max}$ (Fig. 5(b)).

To report the embrittlement of hydrogen charged tests, an embrittlement index EI is typically used. It represents the degradation due

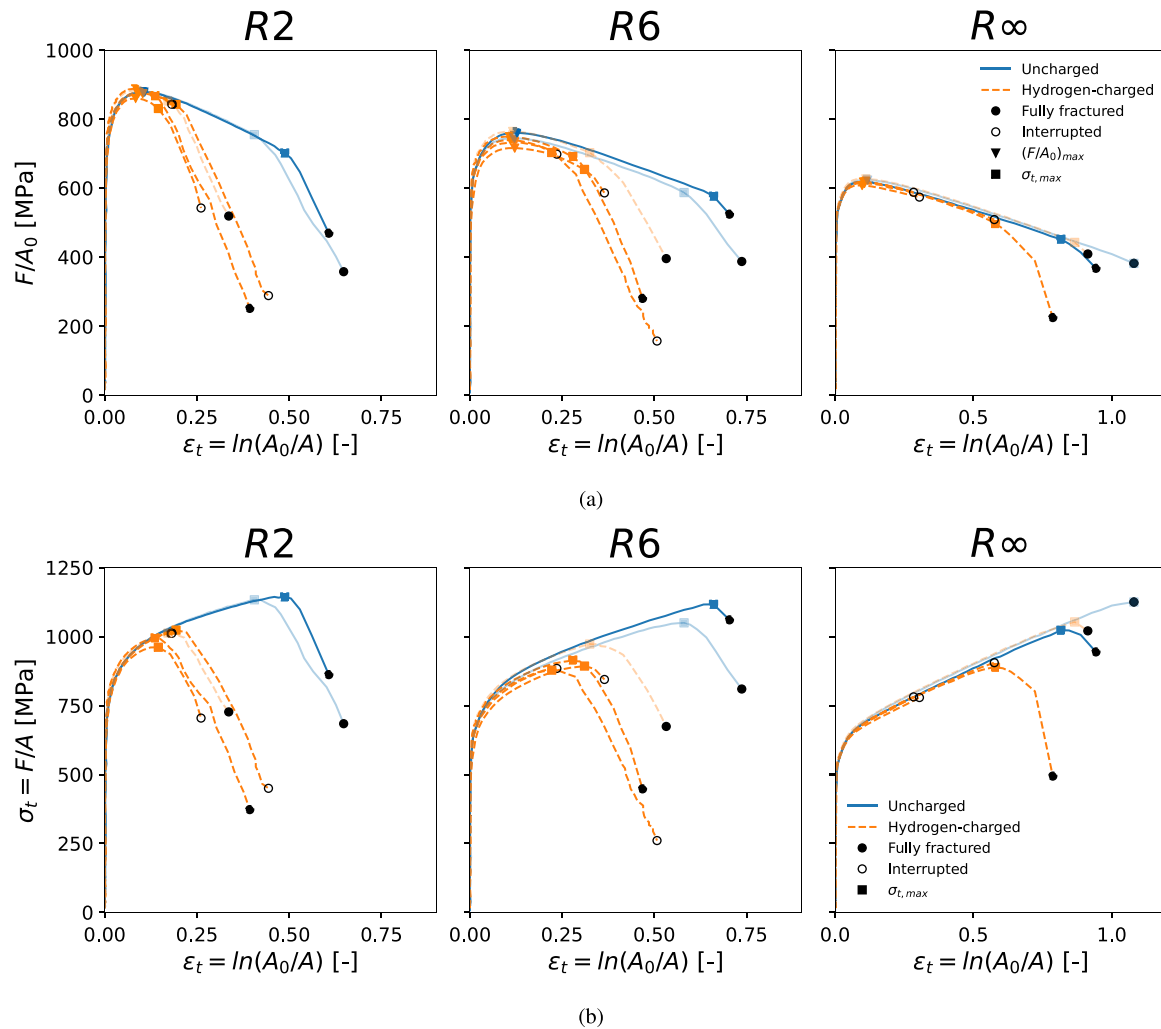


Fig. 5. The (a) normalized load and (b) true stress versus true strain curves of the hydrogen charged and uncharged samples. A significant loss of ductility can be observed for all three specimen geometries. Samples that have not been scanned using X-ray micro-CT are shown more transparent.

Table 2

Characteristic values of the macroscopic response of hydrogen charged and uncharged samples with different geometries. Average and standard deviation is reported.

Notch	Condition	$(F/A_0)_{max}$ [MPa]	ϵ_t at $(F/A_0)_{max}$ [-]	ϵ_c [-]	ϵ_f [-]	\mathcal{L}
R2	Air	879 ± 1	0.11 ± 0.00	0.45 ± 0.06	0.89 ± 0.02	0.84 ± 0.02
	Hydrogen	876 ± 11	0.09 ± 0.01	0.16 ± 0.03	0.48 ± 0.02	0.8 ± 0.05
R6	Air	753 ± 11	0.12 ± 0.01	0.62 ± 0.06	1.07 ± 0.05	0.7 ± 0.02
	Hydrogen	741 ± 18	0.11 ± 0.01	0.28 ± 0.05	0.72 ± 0.08	0.73 ± 0.02
$R\infty$	Air	621 ± 3	0.11 ± 0.01	0.95 ± 0.19	1.32 ± 0.01	0.54 ± 0.01
	Hydrogen	617 ± 7	0.11 ± 0.01	0.72 ± 0.20	1.01 ± 0.18	0.54 ± 0.01

to hydrogen charging of a certain quantity with respect to uncharged samples:

$$EI_{quantity}[\%] = \frac{quantity_{air} - quantity_H}{quantity_{air}} * 100 \% \quad (6)$$

The quantities in Table 2 can be converted into embrittlement indices that quantify the effect of hydrogen charging on the strength and ductility properties, as shown in Fig. 6. Clearly, the strength appears unaffected, while there is a significant degradation in ductility since all strain characteristics are reduced due to the presence of hydrogen, with the most degradation observed for ϵ_c , followed by ϵ_f , and ϵ_t at $(F/A_0)_{max}$. Furthermore, an increasing embrittlement is observed with increasing stress triaxiality since there is up to 60 % of reduction in ϵ_c for R2.

Fig. 7 demonstrates the plastic anisotropy of the material, plotted up to the point of maximum true stress. There is no difference in trend

between the hydrogen charged and the uncharged samples. This is also confirmed by the determination of the Lankford coefficient \mathcal{L} at a true strain of 0.1 (Table 2), where no significant difference was detected. Note that the multiaxial stress state affects the Lankford coefficient values. The final dimensions of the fracture surface are also featured on Fig. 7, showing that the plasticity trend deviates upon macroscopic crack initiation. This is not surprising, given that the fracture process becomes dominant.

Given the above, the macromechanical results suggest that hydrogen definitely accelerates fracture, yet has no distinguishable effect on the macroscopic plasticity. Illustrative fracture surfaces of an uncharged and hydrogen charged R6 specimen, obtained by scanning electron microscopy, are given in Fig. 8. The uncharged specimens feature the expected ductile dimples, while regions of quasi-cleavage are observed on the hydrogen charged specimens. Similar findings apply

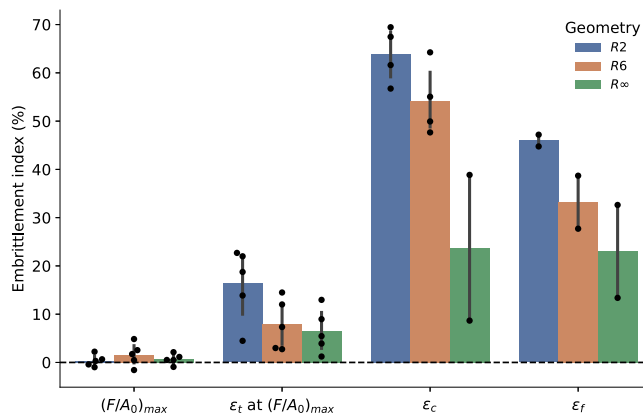


Fig. 6. Degradation of mechanical properties due to hydrogen charging, in the form of embrittlement indices (Eq. (6)).

to the other geometries. MnS inclusions were observed on the fracture surface for both the uncharged and hydrogen charged specimens.

3.2. X-ray micro-CT: microscopic observations

The goal of this section is to reveal the fracture mechanisms using X-ray micro-CT in a qualitative way.

3.2.1. Fracture process in hydrogen charged samples: interrupted tests

To reveal the fracture process in hydrogen charged samples, three tensile tests per notch configuration were terminated before total failure (Fig. 5), and X-ray micro-CT scanned. For each sample, a representative slice in the L-S plane and the L-T plane of the raw data is presented in Figs. 9 and 10, respectively, together with the true strain in the minimal notch cross section (Eq. (2)). Note that other sections will have experienced less strain. Also keep in mind that while the crack might have reached the surface in a specifically shown L-T plane, it is possible that the specimen is not completely fractured yet.

Damage, represented by voids, initiates at the center near the weakest section. Remarkably, voids tend to initiate in a line along the L direction. This phenomenon is called ‘necklace formation’ and has been associated with steels containing elongated inclusions [11]. In agreement with previous studies investigating uncharged steel [47], this phenomenon is favored at lower stress triaxiality. Accordingly, the development of voids is a result of not only plastic strain and stress triaxiality, but also impacted by the microstructure.

A comparison between the slices in the L-T and L-S plane reveals that crack propagation is predominant in the T direction. This can be attributed to the presence of MnS inclusions in the microstructure, since it has been reported that voids nucleated at MnS inclusions can inherit the elongated shape upon sufficient plastic deformation [9]. Further deformation causes void coalescence of the largest voids. Multiple features of regular ductile failure are observed in the deformed hydrogen charged samples. While brittle fracture is typically associated with a limited amount of void development due to the limited plasticity, it is clear that this is not the case for the here reported test results.

3.2.2. Comparison of fracture behavior of hydrogen charged versus uncharged specimens: fully fractured tests

X-ray micro-CT scanning of fully fractured specimens reveals the ductile damage at failure. While the fracture surface is evidently an important signature for the fracture process, damage underneath the fracture surface can also provide important insights. The difference in fracture between hydrogen charged and uncharged specimens is shown in Fig. 11. Note that, while both specimen halves were scanned, only one halve is shown for illustrative purposes.

It is clear that in both test conditions, necklace formation occurs and dominating void growth in the T direction is evident. However, hydrogen charging seems to result in significantly more damage, both directly underneath the fracture surface, but also at regions further away that experienced smaller strains. Moreover, the void shape appears to be altered, as the hydrogen charged samples feature increased lateral void growth, particularly in the S-direction.

Finally, for hydrogen charged specimens, surface cracks are present at machining roughness valleys (see also Figs. 9 and 10), while no surface cracking is observed in air. Clearly, these do not have much to do with the macroscopic failure process occurring at the center, and as a result cannot explain the significantly reduced ductility (Fig. 6).

3.3. X-ray micro-CT: damage quantification

Both the increased damage and the altered void shape due to hydrogen charging can be quantified in terms of geometrical characteristics of individual voids. Histograms showing the distribution of the void equivalent diameter D_{eq} in each sample can be found in Appendix.

Fig. 12 reports the average D_{eq} of the 20 largest voids per sample, which is regularly used to evaluate void growth [26,35,38,50]. By focusing on the 20 largest voids, there is no significant influence of the X-ray micro-CT resolution on the following quantifications [50]. D_{eq} is set out against the longitudinal strain in the minimal cross section ϵ_t for the interrupted tests, and the fracture strain ϵ_f for the fully fractured tests. During void coalescence, the largest voids will link up with each other, affecting the equivalent diameter. Furthermore, in the fully fractured scans, the largest voids are discarded since fracture has occurred along the path featuring the most damage. Nevertheless, a clear increase in damage at lower strains due to hydrogen is observed for all three geometries.

Surprisingly, average diameters D_{eq} in all hydrogen charged samples seem to follow the same trend, regardless of geometry. While it is generally accepted that a larger stress triaxiality will lead to lower void nucleation strains, and larger void growth rates [11,36], this effect is not clearly observed in the hydrogen charged samples. It is hypothesized that the process of void coalescence masks this effect, showing the limitation of this approach [36].

The void volume fraction f versus the local strain ϵ_{loc} for the smooth round bars is presented in Fig. 13 and reveals the strains required for the initiation and growth of damage. While it should be noted that the obtained results overestimate the void nucleation strain due to the limited resolution of the X-ray micro-CT method, they provide an indication of the difference in void nucleation strain due to hydrogen. The minimum strain at which voids are observed in uncharged samples is around 0.7, while voids are observed in hydrogen charged samples at strains of 0.1, approximating the minimal strain in the sample (uniform elongation strain).

In an attempt to provide an improved interpretation of Fig. 13, the Rice–Tracey (RT) model for void growth [51] is used. It describes the spherical void growth of a spherical void in a rigid, perfectly plastic material:

$$\frac{dR}{R} = \alpha \exp\left(\frac{3}{2}\eta\right) d\bar{\epsilon}_p \quad (7)$$

where R is the void radius, η is the stress triaxiality, $\bar{\epsilon}_p$ is the equivalent plastic strain and α is a constant. Upon integration, a logarithmic relation between the ratio of the current and the initial void radius $\frac{R}{R_0}$, and the equivalent plastic strain $\bar{\epsilon}_p$ is obtained. By transforming the void radius R into volume fraction f [52] using

$$\frac{R}{R_0} = \left(\frac{f}{f_0}\right)^{\frac{1}{3}} \quad (8)$$

and assuming that the stress triaxiality η remains constant during void growth for simplicity, the integrated RT model is transformed to

$$\ln\left(\frac{f}{f_0}\right) = 3\alpha \exp\left(\frac{3}{2}\eta\right) \bar{\epsilon}_p \quad (9)$$

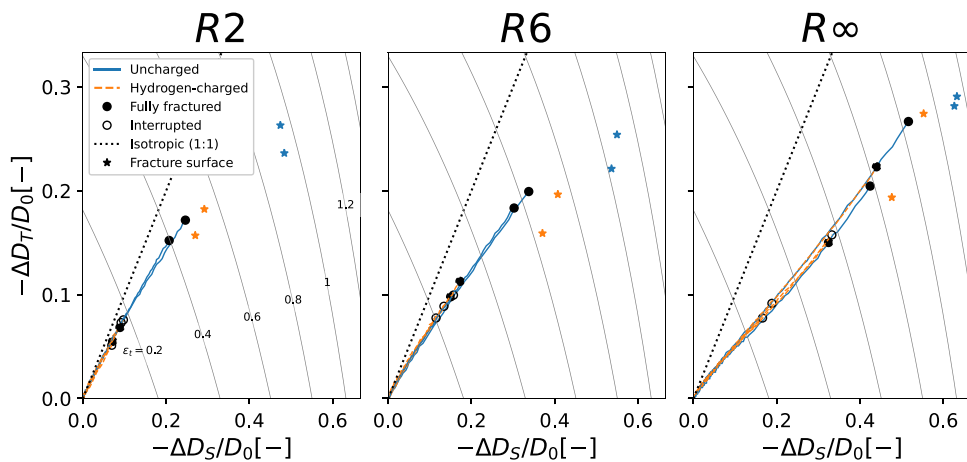


Fig. 7. Lateral contractions in the T direction ($-\Delta D_T$) versus lateral contractions in the S direction ($-\Delta D_S$) during the notched tensile test, indicating that the plastic anisotropy is unchanged due to hydrogen charging. Both lateral contractions are normalized with the initial diameter D_0 . The final dimensions of the fracture surface are displayed with a star.

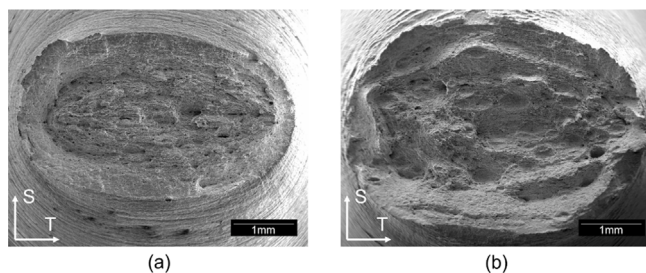


Fig. 8. Scanning electron microscopy images of the fracture surface of (a) uncharged and (b) hydrogen charged R6 specimen, shown at an equal scale.

Note that this only describes void growth, and that extended relations including void nucleation exist [38].

A logarithmic relation between f and ϵ in line with Eq. (9) is also depicted by a regression line in Fig. 13. Low void volume fractions correspond to the void nucleation process and indicate that the void nucleation strain is significantly reduced. The evolution towards higher void volume fractions is associated with void growth and void coalescence. Keeping in mind Eq. (9), the similarity between the slopes for air and hydrogen charged samples indicates that there is no acceleration of the void growth process due to hydrogen. In other words, upon nucleation of a void, the additional strain required for a certain void volume growth is unchanged.

The average void aspect ratios as a function of the equivalent diameter D_{eq} are presented in Fig. 14. It is rationalized that the axis with equivalent diameter D_{eq} also represents the lifetime of a void, going from void nucleation (left) over void growth to void coalescence (right).

First comparing the aspect ratios for uncharged samples with different geometries, reveals that for higher stress triaxiality, voids are less elongated in the T direction, indicated by a larger dS/dT and dL/dT aspect ratio. This observation of more spherical void formation for higher triaxiality can be attributed to the reduced necklace formation.

In addition, it appears that for each individual geometry, all hydrogen charged samples follow similar trends regarding the aspect ratio, even though more strained samples feature larger voids. This observation reinforces the concept of using D_{eq} as the void lifetime, and motivates the idea that a single scan per notch and test condition is enough to visualize the characteristic behavior of a void with respect to its shape. In other words, the results suggest that a scan of the damage in a fractured sample can be used for assessing the void shape during the full deformation process.

Finally, the void shape is significantly affected due to hydrogen charging. In particular, a large hydrogen-induced increase in dS/dL for all stress triaxialities suggests that hydrogen accelerates void growth in the S direction. Further, for the largest stress triaxiality a substantial decrease in aspect ratio dL/dT is observed, indicating that hydrogen enhances void growth also in the T direction under a triaxial stress state. However, this behavior is not seen for lower triaxialities.

4. Discussion

From the results described above, it is clear that a hydrogen concentration of 0.89 wppm does not affect the macroscopic plasticity (including the plastic anisotropy) in the investigated X70 steel. In contrast, damage evolution is clearly affected, both in terms of macroscopic failure strain and of micromechanical indications.

From a macromechanical point of view, an increased embrittlement is observed with increasing stress triaxiality for all investigated strain values (Fig. 6). This trend is also reported in other studies [53–56] and is typically attributed to stress-assisted diffusion causing a higher hydrogen concentration for a larger triaxiality, leading to more embrittlement.

Notably, the slices of hydrogen charged samples in the L-S and L-T plane (Figs. 9 and 10) are similar to the cross-section images in the study of Benzerga et al. [9] who investigated crack growth anisotropy in uncharged X52 pipeline steel. Coalescence seems to occur along 45° in the L-S plane. While this suggests internal shearing coalescence, Benzerga et al. [9] advocate that is a consequence of the anisotropy, rather than an inherent feature of the crack propagation which is still dominated by internal necking coalescence. According to their study, in the ligament between two elongated cracks that are on parallel L-T slices, plane strain prevails which favors shearing and ultimately leads to a zigzag crack path in the L-S plane. Although literature reports that hydrogen could change the coalescence mechanism from internal necking to internal shearing in certain conditions [18], the observed similarity with the crack behavior in Benzerga et al. [9] indicates that internal necking is still the main mechanism responsible for crack propagation which is predominant in the T direction in the hydrogen charged samples reported here. The X-ray micro-CT scans suggest that the fracture process in hydrogen charged samples might also be governed by the normal ductile failure processes (void nucleation, growth and coalescence), yet potentially accelerated due to the presence of hydrogen.

Because the strain at maximum normalized load is reduced due to hydrogen (Fig. 6), and damage is observed at strains close to the uniform elongation strain (Fig. 13), it is suggested that void nucleation

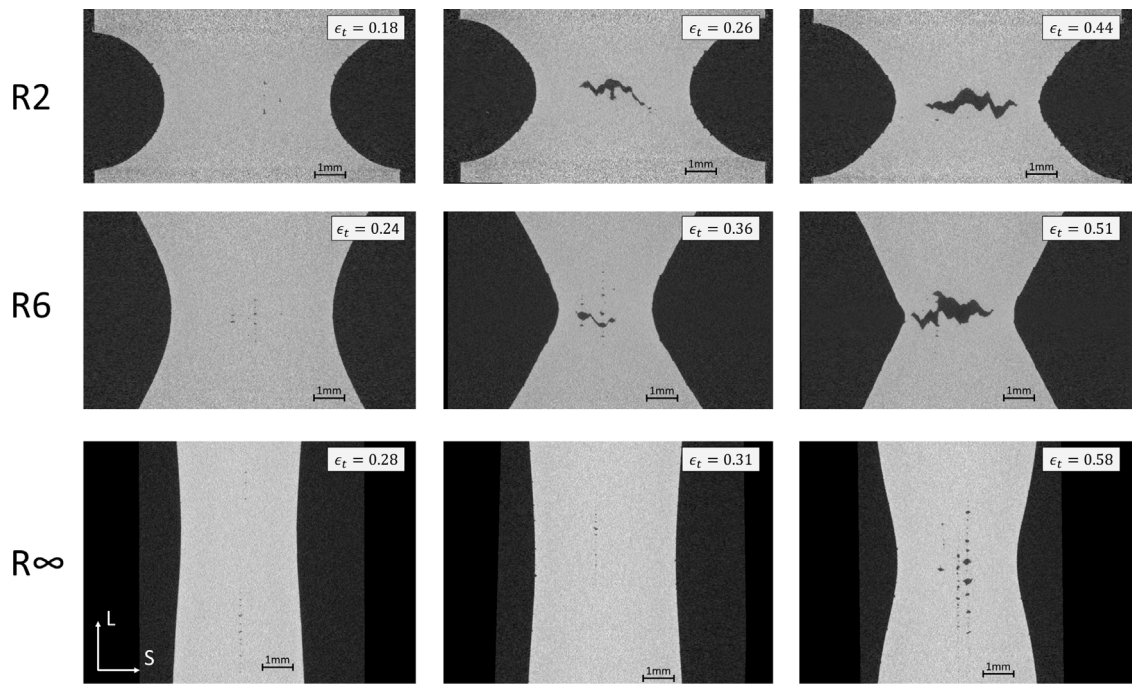


Fig. 9. 2D slices (L-S plane) of the reconstructed X-ray volumes of the interrupted hydrogen charged tensile tests. For each geometry, the strain increases from left to right.

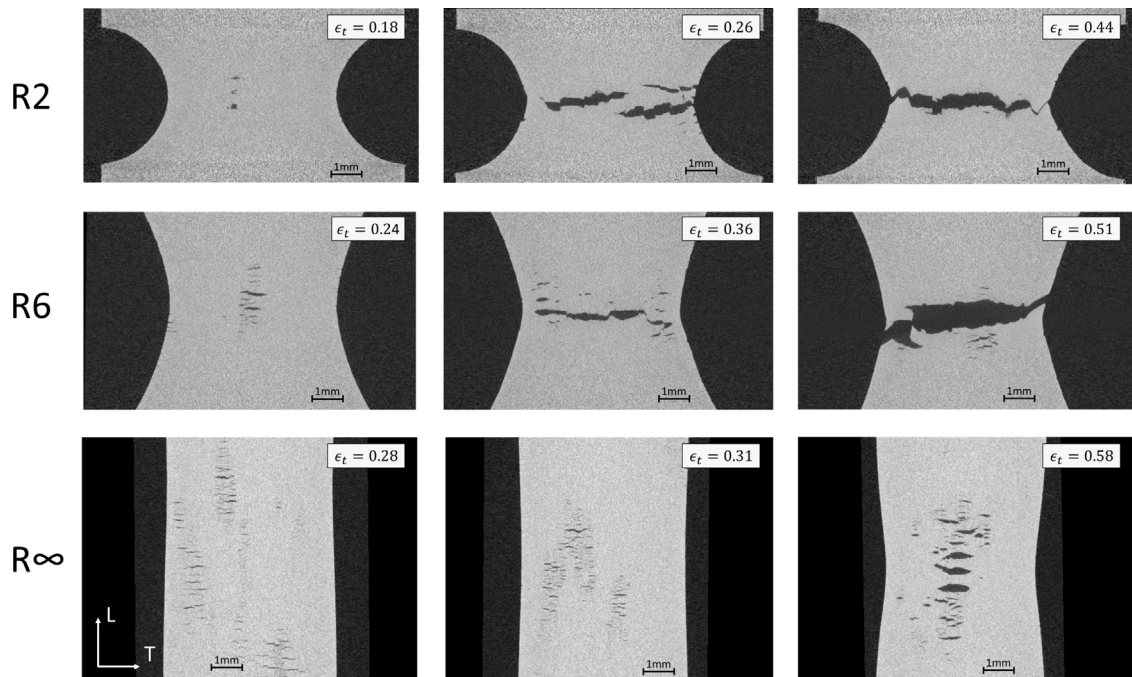


Fig. 10. 2D slices (L-T plane) of the reconstructed X-ray volumes of the interrupted hydrogen charged tensile tests. For each geometry, the strain increases from left to right.

in hydrogen charging is significantly accelerated compared to normal ductile failure. The data suggests that the void nucleation strain in hydrogen is likely to be lower than the uniform elongation strain, while damage is not yet present at this point in uncharged steel. This observation is in agreement with the concept of HESIV, since an hydrogen-induced increase in the vacancy cluster density leads to enhanced nanovoid formation and eventually to accelerated void nucleation [8]. Because of the aligned location of damage initiation, it is hypothesized that void nucleation in both uncharged and hydrogen charged conditions occurs at the elongated MnS inclusions in the banded microstructure. This is in agreement with the work of Hejazi

et al. [57]. Note that while there clearly is some damage at this point, it only has a limited effect on ϵ_t at $(F/A_0)_{max}$, resulting in a lower relative degradation compared to ϵ_c or ϵ_f (Fig. 6).

Regarding void growth, it is unclear whether the increased average equivalent diameter (Fig. 12) is a result of purely the acceleration of void nucleation, or due to an additional acceleration of the void growth process. However, the similar slope of the void volume fraction versus the local strain in Fig. 13 for uncharged and hydrogen charged samples suggests that the process of void growth is not accelerated (or at least the acceleration of void growth is of much lesser significance than the acceleration of void initiation). Further, the investigation of the

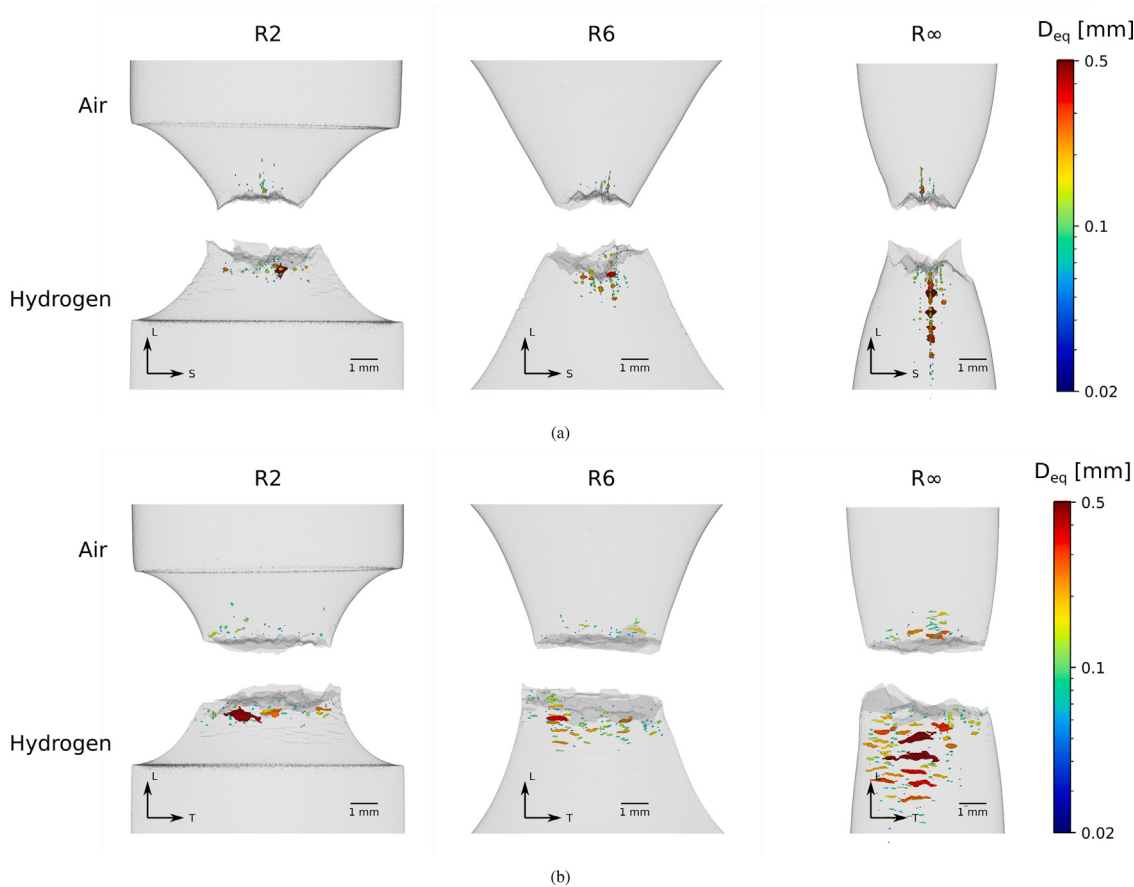


Fig. 11. Thresholded volumes of uncharged (top) and hydrogen charged (bottom) specimens in the (a) L-S plane and (b) L-T plane. Damage is visualized based on the equivalent diameter.

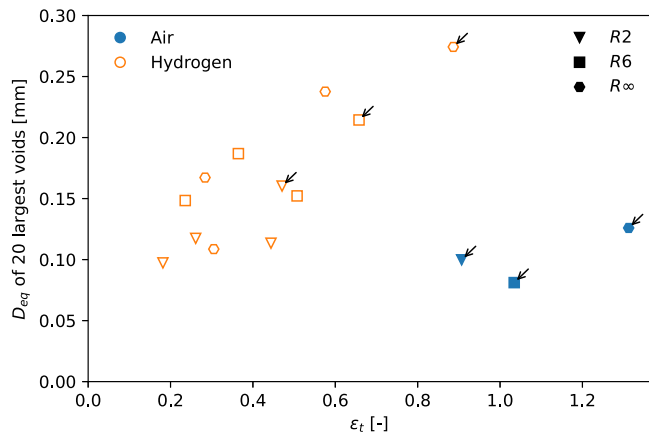


Fig. 12. The average equivalent diameter of the 20 largest voids of each test versus the true strain in the minimal cross section ϵ_t for the interrupted tests, and the fracture strain ϵ_f for the fully fractured tests. Fully fractured samples are indicated with an arrow.

void morphology shows that hydrogen charging results in voids with larger dimensions in the S direction, and for high stress triaxiality in T direction, relative to the loading direction L. Therefore, it can be assumed that the presence of hydrogen enhances lateral void growth for all stress triaxialities. Since the diameter contraction is highest in the S direction (Fig. 7), hydrogen enhanced void growth in the S direction is especially disadvantageous since it will lead to accelerated fracture. The fact that hydrogen enhanced lateral void growth is more prominent in both directions for higher stress triaxialities, may be an explanation

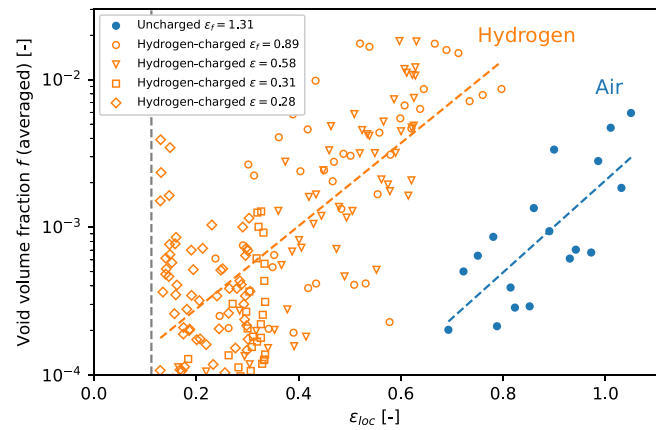


Fig. 13. The void volume fraction f for the smooth round bars (R_∞) as a function of the local strain ϵ_{loc} in each cross-sectional slice. The vertical dashed line corresponds to the uniform elongation strain converted to true strain (which was similar for air tested and hydrogen charged specimens).

for the increased embrittlement with increased triaxiality, and can be associated with the HELP mechanism. Even so, the enhanced lateral void growth could be a consequence of the stress-assisted diffusion, or could be attributed to an additional change in the fracture mechanism.

Finally, similarities in the slope of the stress versus true strain curve after the critical strain (Fig. 5) might be an indication that void coalescence is unchanged. In addition, the similar zig-zag crack path in

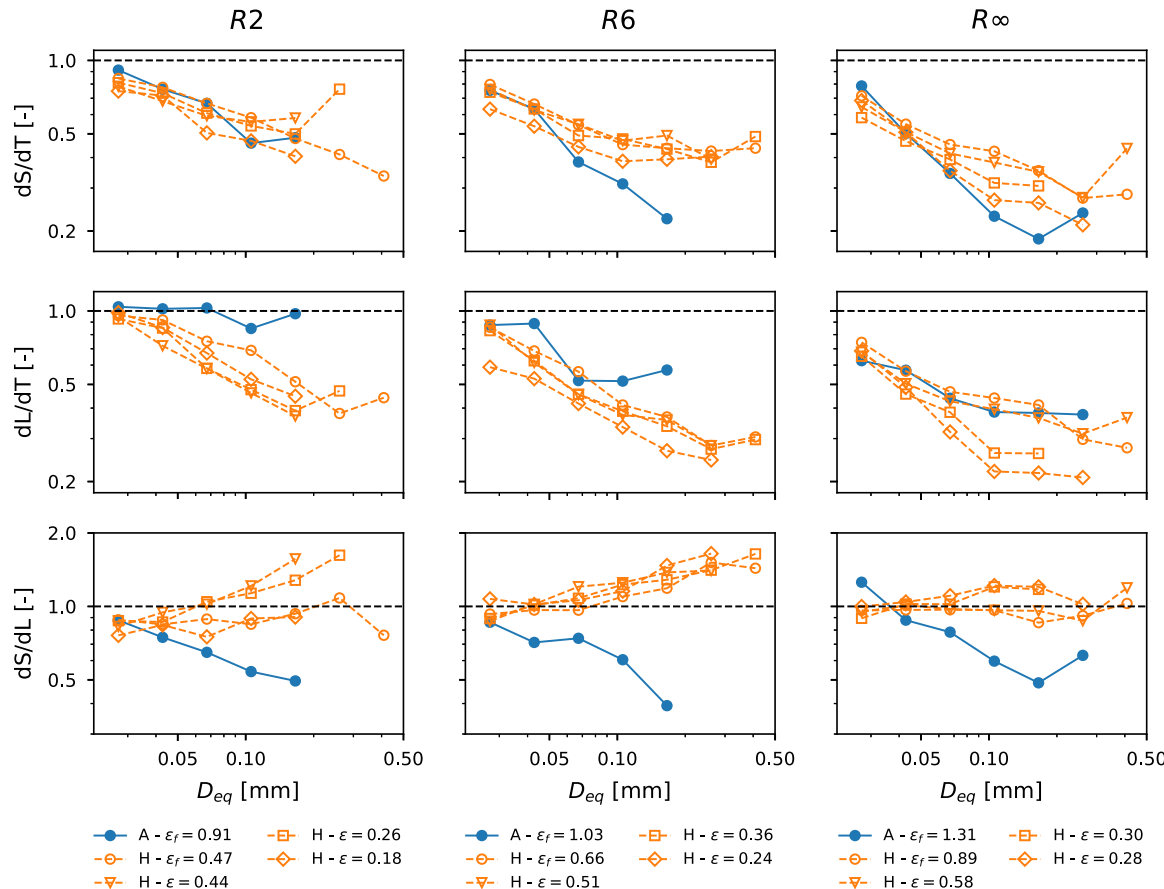


Fig. 14. The aspect ratios of the voids per sample, averaged per equivalent diameter D_{eq} . ‘A’ refers to ‘Air’ and ‘H’ to ‘hydrogen charged’ specimens.

the L-S plane (Fig. 11(a)) for both test conditions suggests unchanged coalescence mechanisms. Consequently, quantifying the embrittlement based on ϵ_c suggests more degradation compared to ϵ_f (Fig. 6).

Given the above, accelerated failure due to hydrogen in the tested X70 pipeline steel can be attributed to at least two aspects: (i) void nucleation at lower strains, and (ii) hydrogen enhanced lateral void growth. This is valid for all studied stress triaxiality values. The acceleration of these processes, together with the observed quasi-cleavage on the fracture surfaces (Fig. 8) point towards the plasticity dominated HE mechanisms HELP and HESIV, and support the hypothesis by Merson et al. [3], Martin et al. [7] and Nagumo et al. [8] that hydrogen embrittlement can be explained by ductile effects. Accordingly, the development of a micromechanics-inspired numerical model for predicting hydrogen embrittlement based on the plasticity dominated mechanisms of HE should keep both observations in mind.

5. Conclusions

The fracture process in API 5L X70 steel, both in air and hydrogen charged, smooth and notched round bar tensile tests has been investigated through the macroscopic responses and micromechanical indications from X-ray micro-CT. The effect of a hydrogen concentration of 0.89 wppm on plasticity and damage behavior for various stress triaxialities has been assessed. The macromechanical plastic behavior including plastic anisotropy is unaffected, but various strains characterizing deformation behavior are significantly reduced due to hydrogen. For higher stress triaxiality, more embrittlement was observed, with up

to 60 % reduction in critical strain for the specimens with the sharpest notches.

The fracture process in hydrogen charged samples featured void nucleation in lines along the loading direction, with subsequent void growth and coalescence. X-ray micro-CT revealed that hydrogen affects the fracture process in two ways. First, hydrogen induces void nucleation at significantly lower strains. It is likely that the presence of hydrogen caused damage initiation prior to maximum load (at a strain level below the uniform elongation strain). Second, hydrogen induces voids whose major axis is more perpendicular to the loading direction, but the void volume growth itself does not appear accelerated. Both observations are valid for all tested stress triaxialities, and contribute to the well-known ductility loss. The increased embrittlement with increasing stress triaxialities can be explained by an increased hydrogen enhanced lateral void growth in both directions, an increased hydrogen concentration resulting from the stress-assisted diffusion, or a combination of both. The results correspond to the plasticity dominated HE theories Hydrogen Enhanced Localized Plasticity (HELP) and Hydrogen Enhanced Strain-Induced Vacancies (HESIV), that explain hydrogen embrittlement as an acceleration of ductile processes.

Due to the complexity of the microstructure of the steel, quantifying the aforementioned effects would be tedious work using conventional metallographic slices, and was significantly facilitated by means of the X-ray micro-CT analyses. The presented results can assist the development and calibration of numerical models for describing hydrogen embrittlement, since the presence and evolution of damage can be related with porosity-based continuum damage models.

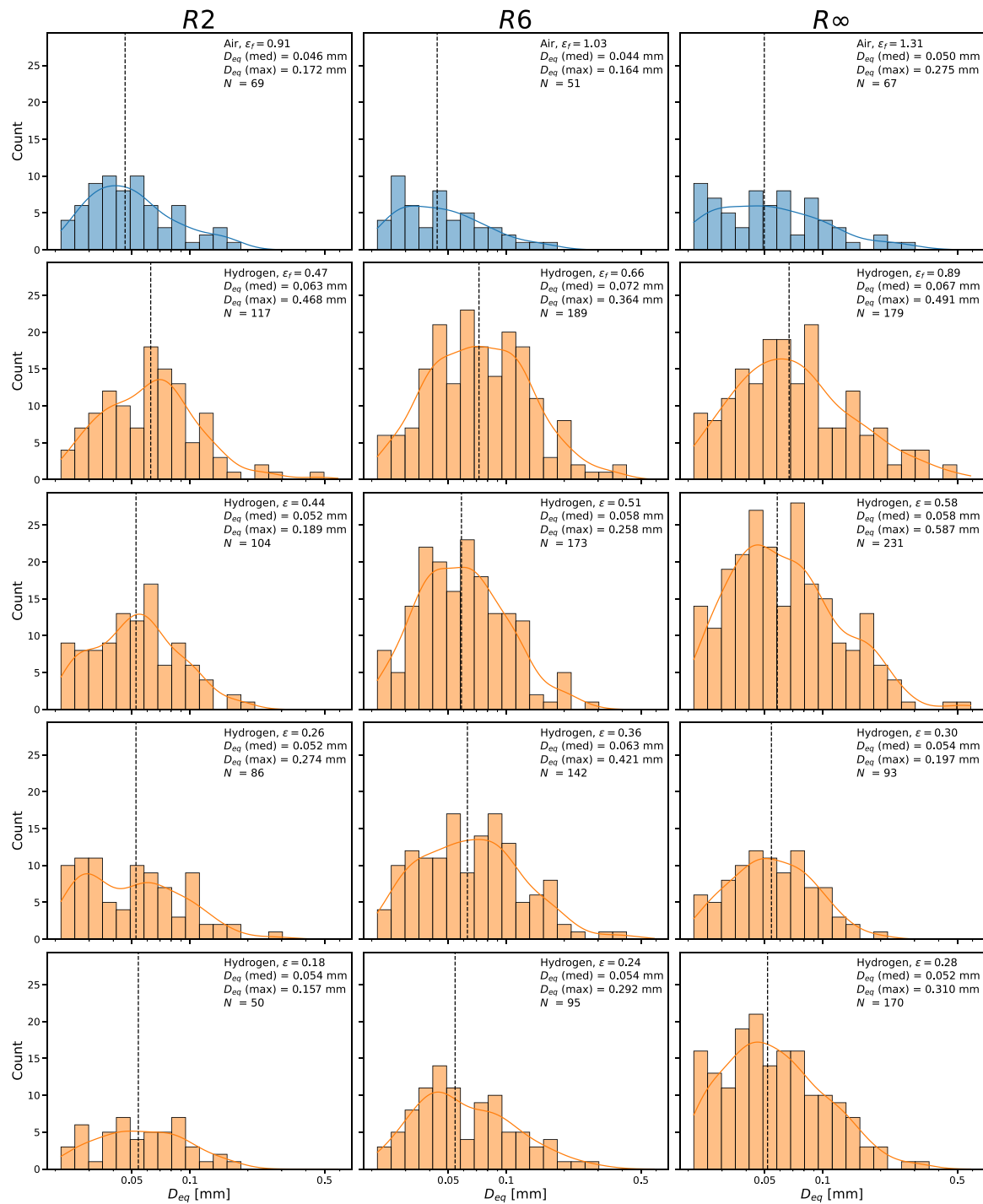


Fig. A.15. The distribution of the void equivalent diameter D_{eq} in each sample. The median value is indicated with a vertical dotted line.

CRediT authorship contribution statement

Robin Depraetere: Methodology, Investigation, Writing – original draft. **Wim De Waele:** Conceptualization, Supervision, Writing – review & editing. **Margo Cauwels:** Methodology, Investigation, Writing – review & editing. **Tom Depover:** Conceptualization, Supervision, Writing – review & editing. **Kim Verbeken:** Conceptualization, Supervision, Writing – review & editing, Funding acquisition. **Matthieu Boone:** Methodology, Writing – review & editing. **Stijn Hertelé:** Conceptualization, Supervision, Writing – review & editing, Funding acquisition.

Declaration of competing interest

The authors declare that they have no known competing financial interests or personal relationships that could have appeared to influence the work reported in this paper.

Data availability

The processed data (X-ray volumes) are uploaded on a public data repository: <https://doi.org/10.17605/OSF.IO/WKHG3>.

Acknowledgments

The authors acknowledge the support from Research Foundation - Flanders (FWO) via grant G056519N. Also, the UGent Special Research Funds (BOF) is acknowledged (grants BOF15/BAS/062, BOF20/BAS/121 and BOF19/GOA/026), including the financial support to the Centre of Expertise UGCT (BOF.EXP.2017.0007). The authors wish to thank the senior postdoctoral fellowship of the Research Foundation - Flanders (FWO) via grant 12ZO420N. Finally, Iván Josipovic is acknowledged for his assistance with performing the X-ray micro-CT scans, and Dante Delanote, Viktor Noppe and Jakob Mertens for their assistance with the execution of the tensile tests.

Data availability statement

The raw data that support the findings of this study are available from the corresponding author upon reasonable request. The processed X-ray volumes are available to download from Open Science Framework [46].

Appendix. Void size distributions

See Fig. A.15.

References

- [1] A. Laureys, R. Depraetere, M. Cauwels, T. Depover, S. Hertelé, K. Verbeken, Use of existing steel pipeline infrastructure for gaseous hydrogen storage and transport: A review of factors affecting hydrogen induced degradation, *J. Nat. Gas Sci. Eng.* 101 (2022) 104534, <http://dx.doi.org/10.1016/j.jngse.2022.104534>.
- [2] W. Johnson, On some remarkable changes produced in iron and steel by the action of hydrogen and acids, in: *Proceedings of the Royal Society of London*, 1875, pp. 168–179.
- [3] E. Merson, P. Myagkikh, G. Klevtsov, D. Merson, A. Vinogradov, Effect of fracture mode on acoustic emission behavior in the hydrogen embrittled low-alloy steel, *Eng. Fract. Mech.* 210 (2019) 342–357, <http://dx.doi.org/10.1016/j.engfracmech.2018.05.026>.
- [4] M.B. Djukic, G.M. Bakic, V. Sijacki Zeravcic, A. Sedmak, B. Rajicic, The synergistic action and interplay of hydrogen embrittlement mechanisms in steels and iron: Localized plasticity and decohesion, *Eng. Fract. Mech.* (2019) <http://dx.doi.org/10.1016/j.engfracmech.2019.106528>.
- [5] M. Nagumo, Fundamentals of Hydrogen Embrittlement, 2016, pp. 1–239, <http://dx.doi.org/10.1007/978-981-10-0161-1>.
- [6] S.P. Lynch, Hydrogen embrittlement (HE) phenomena and mechanisms, in: *Stress Corrosion Cracking: Theory and Practice* (i), 2011, pp. 90–130, <http://dx.doi.org/10.1533/9780857093769.1.90>.
- [7] M.L. Martin, J.A. Fenske, G.S. Liu, P. Sofronis, I.M. Robertson, On the formation and nature of quasi-cleavage fracture surfaces in hydrogen embrittled steels, *Acta Mater.* 59 (4) (2011) 1601–1606, <http://dx.doi.org/10.1016/j.actamat.2010.11.024>.
- [8] M. Nagumo, K. Takai, The predominant role of strain-induced vacancies in hydrogen embrittlement of steels: Overview, *Acta Mater.* 165 (2019) 722–733, <http://dx.doi.org/10.1016/j.actamat.2018.12.013>.
- [9] A.A. Benzerga, J. Besson, A. Pineau, Anisotropic ductile fracture: Part I: Experiments, *Acta Mater.* 52 (15) (2004) 4623–4638, <http://dx.doi.org/10.1016/j.actamat.2004.06.020>.
- [10] W. Wciślik, S. Lipiec, Void-induced ductile fracture of metals: Experimental observations, *Materials* 15 (18) (2022) 6473, <http://dx.doi.org/10.3390/ma15186473>.
- [11] A. Pineau, A.A. Benzerga, T. Pardoen, Failure of metals I: Brittle and ductile fracture, *Acta Mater.* 107 (2016) 424–483, <http://dx.doi.org/10.1016/j.actamat.2015.12.034>.
- [12] H.J. Cialone, R.J. Asaro, The role of hydrogen in the ductile fracture of plain carbon steels, *Metall. Trans. A* 10 (1979) 367–375.
- [13] R. Garber, I.M. Bernstein, A.W. Thompson, Effect of hydrogen on ductile fracture of spheroidized steel, *Scr. Metall.* 10 (4) (1976) 341–345.
- [14] D.I. Kwon, R.J. Asaro, Hydrogen-assisted ductile fracture in spheroidized 1518 steel, *Acta Metall. Mater.* 38 (8) (1990) 1595–1606, [http://dx.doi.org/10.1016/0956-7151\(90\)90127-3](http://dx.doi.org/10.1016/0956-7151(90)90127-3).
- [15] T. Matsuo, N. Homma, S. Matsuoka, Y. Murakami, Effect of hydrogen and prestrain on tensile properties of carbon steel SGP (0.078 C-0.012 Si-0.35 Mn, mass%) for 0.1 MPa hydrogen pipelines, *Nihon Kikai Gakkai Ronbunshu A Hen/Trans. Japan Soc. Mech. Eng. A* 74 (744) (2008) 1164–1173, <http://dx.doi.org/10.1299/kikaia.74.1164>.
- [16] D.C. Ahn, P. Sofronis, R.H. Dodds, On hydrogen-induced plastic flow localization during void growth and coalescence, *Int. J. Hydrogen Energy* 32 (16) (2007) 3734–3742, <http://dx.doi.org/10.1016/j.ijhydene.2006.08.047>.
- [17] M.Q. Chandler, M.F. Horstemeyer, M.I. Baskes, P.M. Gullett, G.J. Wagner, B. Jelinek, Hydrogen effects on nanovoid nucleation in face-centered cubic single-crystals, *Acta Mater.* 56 (1) (2008) 95–104, <http://dx.doi.org/10.1016/j.actamat.2007.09.012>.
- [18] H. Yu, J.S. Olsen, J. He, Z. Zhang, Hydrogen-microvoid interactions at continuum scale, *Int. J. Hydrogen Energy* 43 (21) (2018) 10104–10128, <http://dx.doi.org/10.1016/j.ijhydene.2018.04.064>.
- [19] T. Luo, C. Huang, X. Gao, An investigation of the effect of hydrogen on ductile fracture using a unit cell model, *Int. J. Hydrogen Energy* 44 (16) (2019) 8627–8640, <http://dx.doi.org/10.1016/j.ijhydene.2019.02.069>.
- [20] A. Diaz, J. Alegre, I.I. Cuesta, Z. Zhang, Numerical study of hydrogen influence on void growth at low triaxialities considering transient effects, *Int. J. Mech. Sci.* (2019) <http://dx.doi.org/10.1016/j.ijmecsci.2019.105176>.
- [21] H. Yu, J.S. Olsen, A. Alvaro, L. Qiao, J. He, Z. Zhang, Hydrogen informed Gurson model for hydrogen embrittlement simulation, *Eng. Fract. Mech.* 217 (2019) <http://dx.doi.org/10.1016/j.engfracmech.2019.106542>.
- [22] R. Depraetere, W. De Waele, S. Hertelé, Fully-coupled continuum damage model for simulation of plasticity dominated hydrogen embrittlement mechanisms, *Comput. Mater. Sci.* 200 (2021) 110857, <http://dx.doi.org/10.1016/j.commatsci.2021.110857>.
- [23] M. Lin, H. Yu, Y. Ding, V. Olden, A. Alvaro, J. He, Z. Zhang, Simulation of ductile-to-brittle transition combining complete Gurson model and CZM with application to hydrogen embrittlement, *Eng. Fract. Mech.* 268 (2022) <http://dx.doi.org/10.1016/j.engfracmech.2022.108511>.
- [24] S. Huang, Y. Zhang, C. Yang, H. Hu, Fracture strain model for hydrogen embrittlement based on hydrogen enhanced localized plasticity mechanism, *Int. J. Hydrogen Energy* 45 (46) (2020) 25541–25554, <http://dx.doi.org/10.1016/j.ijhydene.2020.06.271>.
- [25] M. Asadipoor, J. Kadkhodapour, A. Pourkamali Anaraki, S.M. Sharifi, A.C. Darabi, A. Barnoush, Experimental and numerical investigation of hydrogen embrittlement effect on microdamage evolution of advanced high-strength dual-phase steel, *Met. Mater. Int.* (2020) <http://dx.doi.org/10.1007/s12540-020-00681-1>.
- [26] E. Maire, S. Grabon, J. Adrien, P. Lorenzino, Y. Asanuma, O. Takakuwa, H. Matsunaga, Role of hydrogen-charging on nucleation and growth of ductile damage in austenitic stainless steels, *Materials* 12 (9) (2019) 1–15, <http://dx.doi.org/10.3390/ma2091426>.
- [27] L.S. Morrissey, S.M. Handigan, S. Nakhla, Quantifying void formation and changes to microstructure during hydrogen charging: A precursor to embrittlement and blistering, *Metall. Mater. Trans. A* 50 (3) (2019) 1460–1467, <http://dx.doi.org/10.1007/s11661-018-5071-8>.
- [28] M.L. Martin, M. Dadfarnia, A. Nagao, S. Wang, P. Sofronis, Enumeration of the hydrogen-enhanced localized plasticity mechanism for hydrogen embrittlement in structural materials, *Acta Mater.* 165 (2019) 734–750, <http://dx.doi.org/10.1016/j.actamat.2018.12.014>.
- [29] P. Sofronis, Y. Liang, N. Aravas, Hydrogen induced shear localization of the plastic flow in metals and alloys, *Eur. J. Mech. A Solids* 20 (6) (2001) 857–872, [http://dx.doi.org/10.1016/S0997-7538\(01\)01179-2](http://dx.doi.org/10.1016/S0997-7538(01)01179-2).
- [30] J. Xie, R. Zhang, T. Liu, C. Zhou, L.-J. Jia, Effect of initial void shape on void growth of structural steels based on micromechanical RVE models, *J. Mater. Civ. Eng.* 34 (4) (2022) [http://dx.doi.org/10.1061/\(ASCE\)MT.1943-5533.0004150](http://dx.doi.org/10.1061/(ASCE)MT.1943-5533.0004150).
- [31] M. Lugo, M.A. Tschoff, J.B. Jordon, M.F. Horstemeyer, Microstructure and damage evolution during tensile loading in a wrought magnesium alloy, *Ser. Mater.* 64 (9) (2011) 912–915, <http://dx.doi.org/10.1016/j.scriptamat.2011.01.029>.
- [32] A. Das, T. Chowdhury, S. Tarafder, Ductile fracture micro-mechanisms of high strength low alloy steels, *Mater. Des.* 54 (2014) 100–1009, <http://dx.doi.org/10.1016/j.matdes.2013.09.018>.
- [33] C. Landron, E. Maire, O. Bouaziz, J. Adrien, L. Lecarme, A. Bareggi, Validation of void growth models using X-ray microtomography characterization of damage in dual phase steels, *Acta Mater.* 59 (20) (2011) 7564–7573, <http://dx.doi.org/10.1016/j.actamat.2011.08.046>.
- [34] M. Daly, T.L. Burnett, E.J. Pickering, O.C.G. Tuck, F. Léonard, R. Kelley, P.J. Withers, A.H. Sherry, A multi-scale correlative investigation of ductile fracture, *Acta Mater.* 130 (2017) 56–68, <http://dx.doi.org/10.1016/j.actamat.2017.03.028>.
- [35] Y. Madi, J.M. Garcia, H. Proudhon, Y. Shinohara, L. Helfen, J. Besson, T.F. Morgeneyer, On the origin of the anisotropic damage of X100 line pipe steel: Part I—In situ synchrotron tomography experiments, *Integr. Mater. Manuf. Innov.* 8 (4) (2019) 570–596, <http://dx.doi.org/10.1007/s40192-019-00165-0>.
- [36] M. Azman, C. Le Bourlot, A. King, D. Fabrègue, E. Maire, 4D characterisation of void nucleation, void growth and void coalescence using advanced void tracking algorithm on in situ X-ray tomographic data, *Mater. Today Commun.* 32 (2022) 103892, <http://dx.doi.org/10.1016/j.mtcomm.2022.103892>.
- [37] G. Requena, E. Maire, C. Leguen, S. Thuijller, Separation of nucleation and growth of voids during tensile deformation of a dual phase steel using synchrotron microtomography, *Mater. Sci. Eng. A* 589 (2014) 242–251, <http://dx.doi.org/10.1016/j.msea.2013.09.084>.

- [38] T.-S. Cao, E. Maire, C. Verdu, C. Bobadilla, P. Lasne, P. Montmitonnet, P.O. Bouchard, Characterization of ductile damage for a high carbon steel using 3D X-ray micro-tomography and mechanical tests - Application to the identification of a shear modified GTN model, *Comput. Mater. Sci.* 84 (2014) 175–187, <http://dx.doi.org/10.1016/j.commatsci.2013.12.006>.
- [39] American Petroleum Institute, *API Specification 5L - Line Pipe, no. 46*, 2018.
- [40] R. Depraetere, M. Cauwels, W. de Waele, T. Depover, K. Verbeken, S. Hertelé, Calibrating a ductile damage model for two pipeline steels: Method and challenges, *Procedia Struct. Integr.* 28 (2020) 2267–2276, <http://dx.doi.org/10.1016/j.prostr.2020.11.072>.
- [41] M. Cauwels, R. Depraetere, W. De Waele, S. Hertelé, T. Depover, K. Verbeken, Influence of electrochemical hydrogenation parameters on microstructures prone to hydrogen-induced cracking, *J. Nat. Gas Sci. Eng.* 101 (2022) 104533, <http://dx.doi.org/10.1016/j.jngse.2022.104533>.
- [42] P.W. Bridgman, *Studies in Large Plastic Flow and Fracture with Special Emphasis on the Effects of Hydrostatic Pressure*, McGraw-Hill, New York (N.Y.), 1952.
- [43] J.S. Kim, N.O. Larrosa, A.J. Horn, Y.J. Kim, R.A. Ainsworth, Notch bluntness effects on fracture toughness of a modified S690 steel at 150 °C, *Eng. Fract. Mech.* 188 (2018) 250–267, <http://dx.doi.org/10.1016/j.engfracmech.2017.05.047>.
- [44] Z. Shokeir, J. Besson, C. Belhadj, T. Petit, Y. Madi, Edge tracing technique to study post-necking behavior and failure in Al alloys and anisotropic plasticity in line pipe steels, *Fatigue Fract. Eng. Mater. Struct.* (2022) <http://dx.doi.org/10.1111/ffe.13754>.
- [45] B. Masschaele, M. Dierick, D.V. Loo, M.N. Boone, L. Brabant, E. Pauwels, V. Cnudde, L.V. Hoorebeke, HECTOR: A 240kV micro-CT setup optimized for research, in: *Journal of Physics: Conference Series*, Vol. 463, IOP Publishing, 2013, 012012, <http://dx.doi.org/10.1088/1742-6596/463/1/012012>.
- [46] R. Depraetere, W. De Waele, M. Cauwels, T. Depover, K. Verbeken, M.N. Boone, S. Hertelé, [dataset] Influence of stress triaxiality on hydrogen assisted ductile damage in an X70 pipeline steel, 2022, <http://dx.doi.org/10.17605/OSF.IO/WKHG3>.
- [47] A.A. Benzerga, J.B. Leblond, Ductile Fracture by Void Growth to Coalescence, Vol. 44, Elsevier Inc., 2010, pp. 169–305, [http://dx.doi.org/10.1016/S0065-2156\(10\)44003-X](http://dx.doi.org/10.1016/S0065-2156(10)44003-X).
- [48] C. Soret, Strain-Based Design of Pipelines in Extreme Environments (Ph.D. thesis), Materials. Université Paris sciences et lettres, 2017, English. NNT : 2017PSLEM044 . tel-01845069. URL <https://pastel.archives-ouvertes.fr/tel-01845069>.
- [49] Y. Shinohara, Y. Madi, J. Besson, Anisotropic ductile failure of a high-strength line pipe steel, *Int. J. Fract.* 197 (2) (2016) 127–145, <http://dx.doi.org/10.1007/s10704-015-0054-x>.
- [50] C. Landron, E. Maire, J. Adrien, O. Bouaziz, M. Di Michiel, P. Cloetens, H. Suohonen, Resolution effect on the study of ductile damage using synchrotron X-ray tomography, *Nucl. Instrum. Methods Phys. Res. B* 284 (2012) 15–18, <http://dx.doi.org/10.1016/j.nimb.2011.08.069>.
- [51] J.R. Rice, D.M. Tracey, On the ductile enlargement of voids in triaxial stress fields*, *J. Mech. Phys. Solids* 17 (3) (1969) 201–217, [http://dx.doi.org/10.1016/0022-5096\(69\)90033-7](http://dx.doi.org/10.1016/0022-5096(69)90033-7).
- [52] T. Pardoën, F. Delannay, Assessment of void growth models from porosity measurements in cold-drawn copper bars, *Metall. Mater. Trans. A* 29 (7) (1998) 1895–1909, <http://dx.doi.org/10.1007/s11661-998-0014-4>.
- [53] D.A. Koss, Y. Fan, Stress State and Hydrogen-Related Fracture, Tech. rep., 1986, URL <https://apps.dtic.mil/sti/citations/ADA172488>.
- [54] A. Diaz, J.M. Alegre, I.I. Cuesta, Numerical simulation of hydrogen embrittlement and local triaxiality effects in notched specimens, *Theor. Appl. Fract. Mech.* 90 (2017) 294–302, <http://dx.doi.org/10.1016/j.tafmec.2017.06.017>.
- [55] A. Cayón, F. Gutiérrez-Solana, B. Arroyo, J. Álvarez, Hydrogen embrittlement processes in microalloyed steel notched tensile samples, *Theor. Appl. Fract. Mech.* 112 (2020) 102878, <http://dx.doi.org/10.1016/j.tafmec.2020.102878>.
- [56] T.T. Nguyen, N. Tak, J. Park, S.H. Nahm, U.B. Beak, Hydrogen embrittlement susceptibility of X70 pipeline steel weld under a low partial hydrogen environment, *Int. J. Hydrogen Energy* 45 (43) (2020) 23739–23753, <http://dx.doi.org/10.1016/j.ijhydene.2020.06.199>.
- [57] D. Hejazi, A. Calka, D. Dunne, E. Pereloma, Effect of gaseous hydrogen charging on the tensile properties of standard and medium Mn X70 pipeline steels, *Mater. Sci. Technol.* 32 (7) (2016) 675–683, <http://dx.doi.org/10.1080/02670836.2015.1130331>.